ELSEVIER

B-type olivine fabric in the mantle wedge: Insights from high-resolution non-Newtonian subduction zone models

Erik A. Kneller [a,*], Peter E. van Keken [a], Shun-ichiro Karato [b], Jeffrey Park [b]

[a]*Department of Geological Sciences, University of Michigan, Ann Arbor MI 48109, USA*
[b]*Department of Geology and Geophysics, Yale University, New Haven, CT 06520, USA*

Abstract

Several hypotheses have been proposed to explain trench-parallel shear wave splitting in the mantle wedge of subduction zones. These include 3-D flow effects, parallel melt filled cracks, and B-type olivine fabric. We predict the distribution of B-type and other fabrics with high-resolution thermal and stress models of subduction zones. A composite viscous rheology is used that incorporates wet diffusion creep, wet dislocation creep, and a stress-limiting approximated Peierls creep law. Rheological parameters for dislocation and diffusion creep are based on deformation experiments. The effects of variable viscous coupling between the slab and mantle are explored using kinematic boundary conditions that change along the top of the slab. Two end-member models are observed, which depend on the depth of partial viscous coupling between the slab and mantle: (1) deep partial coupling which gives rise to cold, high-stress conditions in the forearc mantle and high-temperature, low-stress conditions in the arc and back-arc mantle (2) full viscous coupling at the base of a 40 km conducting lid which is characterized by high temperature and low stress. The case with deep partial coupling, which produces a better match with attenuation tomography and heat flow, shows a large region with suitable conditions for B-type fabric in the forearc mantle and a rapid transition toward the back-arc to conditions that are more suitable for A-, C-, or E-type fabrics. Full viscous coupling gives rise to high-temperature, low-stress conditions unsuitable for B-type fabric. Our modeling predicts that the best candidates for regions with B-type fabric are the forearc mantle and a cold 10–15 km layer above the slab.
© 2005 Elsevier B.V. All rights reserved.

Keywords: olivine fabric; seismic anisotropy; subduction zone modeling

1. Introduction

Deformation in the mantle wedge of subduction zones causes lattice preferred orientation (LPO) which in turn affects the directional dependence of seismic wave velocity. This provides the potential to map

---

* Corresponding author. Tel.: +1 734 763 5949; fax: +1 734 763 4690.

E-mail addresses: eknreller@umich.edu (E.A. Kneller), keken@umich.edu (P.E. van Keken), shun-ichiro.karato@yale.edu (S. Karato), jeffrey.park@yale.edu (J. Park).

deformation fabric with seismological observations and thus gain insight into the pattern of solid-state flow. The pattern of anisotropy in subduction zones is diverse and poorly understood but advances in mineral physics and new seismic observations provide improved constraints. Deformation experiments have yielded new insights into the diversity of olivine fabric [1,2] and new studies of anisotropy are increasing our knowledge of deformation fabric in the mantle wedge [3,4]. Progress is also being made with seismology toward better constraining the geometry of the slab and subducting crust and the distribution of temperature, water, and partial melt [5,6]. These advances can be coupled with geodynamics to form physically more realistic models of subduction zone processes. This work uses recent deformation experiments and geodynamic models of the mantle wedge to investigate the possibility that water-induced fabric transitions play an important role in controlling the pattern of seismic anisotropy in the mantle wedge.

Seismic anisotropy can be caused by parallel alignment of isotropic layers and cracks in the mantle and crust, and LPO [7,8]. Studies of the distribution of anisotropy in subduction zones suggest that LPO is the dominant cause of seismic anisotropy [7,9,10]. A variety of fabrics have been observed in naturally deformed olivine aggregates from a range of tectonic settings [11–16]. The most common olivine fabric is A-type, which has a fast-axis orientation subparallel to the shear direction [12]. This fabric has been used to explain convergence-parallel fast directions from surface-wave and P_n tomography in mid-ocean ridge systems [8,17]. However, this simple model fails for subduction zones where the fast direction varies with respect to convergence direction and often is trench-parallel [5,10,18–20]. In some cases trench-parallel fast directions may be caused by anisotropy within or beneath the slab. For example, in the Kamchatka forearc, teleseismic SKS splitting is trench-parallel [21], but both receiver functions [22] and shear-wave splitting from events in the slab [23] indicate a trench-normal fast axis with weak splitting. This suggests a trench-normal fast axis in the forearc mantle wedge and a trench-parallel fast axis beneath the slab.
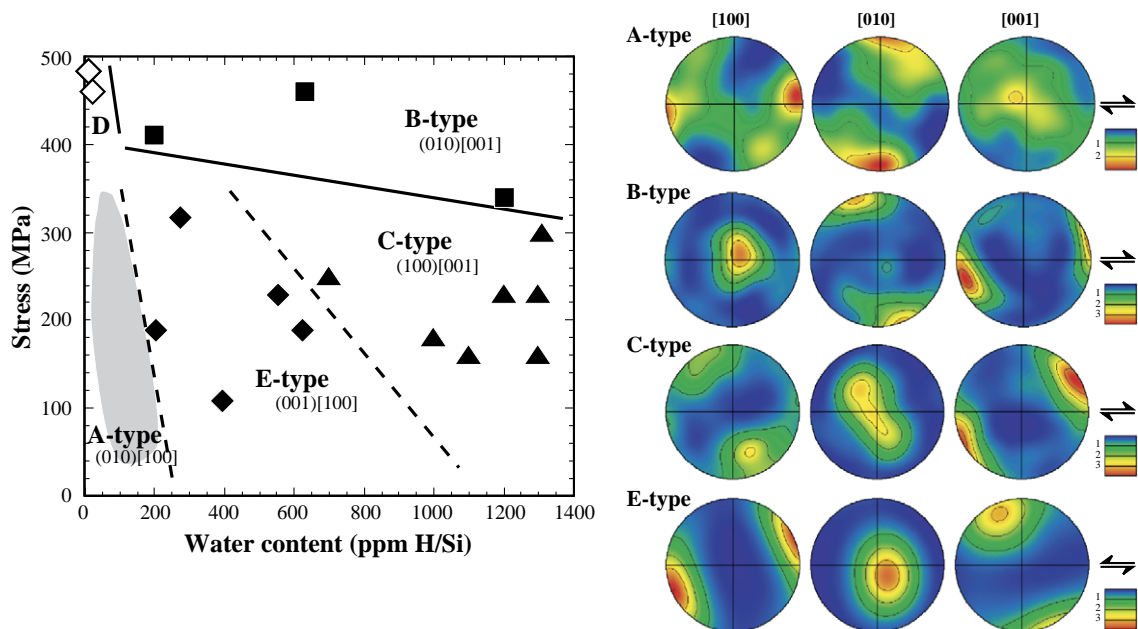

Fig. 1. Fabric map of olivine for high-temperature (1470–1570 K), high-stress experiments (left) [1,2]. Spherical projections of *a*, *b*, and *c* axes are shown on the right. Shear direction is denoted with black arrows. The B-type fabric is observed at high-stress, relatively water-rich conditions and has an [100] (fast axis) orientation that is sub-normal to the shear direction in the shear plane. Data for A-type (gray) are from [1,27]. Data for B-type (squares) and C-type (triangles) are from [1]. Data for D-type (open diamonds) are from [27,28]. Data for E-type (closed diamonds) are from [2].

Several hypotheses have been proposed that use LPO to explain trench-parallel shear wave splitting in the mantle wedge of subduction zones. These hypotheses include LPO controlled by 3-D flow effects [24], olivine fabric transitions [1,25], and strain partitioning via melt networks [26]. The evidence for abundant water in subduction zones [25] suggests that water-induced fabric transitions in olivine is a mechanism common to all subduction environments. However, the diversity of patterns of anisotropy in subduction zones makes it difficult to ascribe a single mechanism and it is possible that a variety of mechanisms are at play.

Recent deformation experiments have explored the influence of a variety of physico-chemical conditions on olivine fabrics [1,2,27,28]. Combined with theory [29] and observations on naturally deformed peridotites [11,13,14,16,30–33] we now have a better idea about the variation of olivine LPO with water content, stress, and temperature. Briefly, the A-type fabric, assumed in the previous interpretation of seismic anisotropy, is a dominant fabric under low stress and low water content, whereas at higher water contents, other types of olivine fabrics become important (B-, C- and E-types) (Fig. 1).

Particularly important is the B-type fabric. For this type of LPO, the seismically fast direction of olivine, [100], is normal to the flow direction in the flow plane (which is the (010) plane of olivine). Consequently, the direction of polarization of the faster S-wave is parallel to the trench if flow in the mantle wedge is similar to 2D cornerflow where flow occurs either in the horizontal or vertical plane. Thus the B-type fabric is of particular importance in explaining trench-parallel fast S-wave polarization in subduction zones. According to both experimental [33] and theoretical [29] studies, the fabric boundary between B-type and C-type (also A- and E-type) fabric is a nearly linear function of temperature and stress and is approximately independent of water content as far as water content exceeds approximately 200 ppm H/Si (Fig. 2).
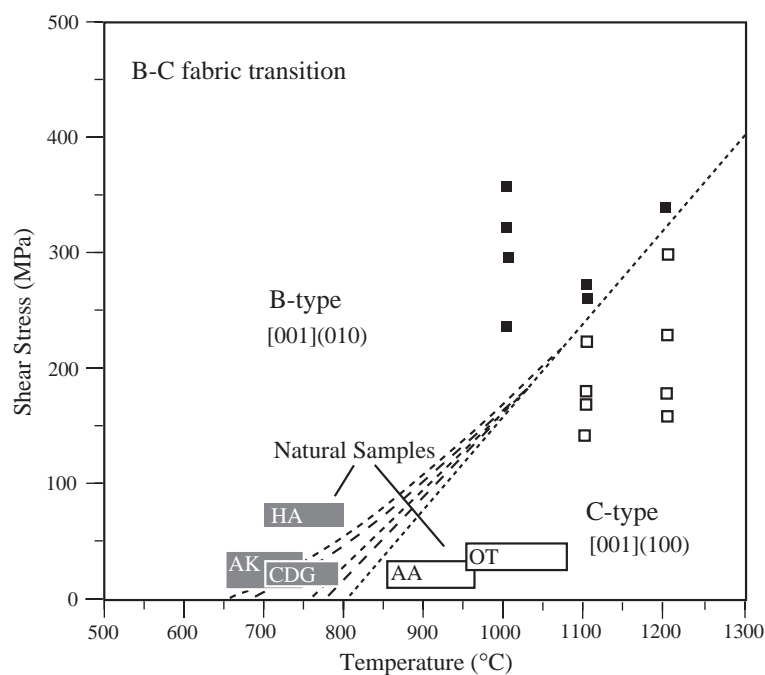

Fig. 2. Fabric map in temperature–stress space [29,33]. The dashed lines show the transition in the dominant slip system and type of olivine fabric for different rheological parameters. The transition temperature at mantle wedge stress (0.1–20 MPa) is predicted to be around 700–800 °C. Experiments are denoted with black squares (B-type) and white squares (C-type). Data on natural samples of B- and C-type fabrics come from Alpe Arami, Switzerland (AA) [13,30]; Otrøy island, Norway [33] (OT); Almklovdalen, Norway [31] Higashi-Akaishi-Yama, Japan [16] (HA); Cima di Gagnone, central Alps [32] (CDG).

In order for a particular fabric to develop several criteria must be satisfied. Firstly, dislocation creep must be the dominant deformation mechanism. In the models presented in this paper, dislocation creep is predicted to be the dominant mechanism for most of the mantle wedge except for the low-strain–rate boundary layer below the overriding plate. Secondly, sufficient strain ($\approx 100\%$) must develop for a given flow geometry. We did not calculate finite strain in this study but instead constrain our fabric predictions to regions with relatively high strain rate ($> 10^{-16}$ s^{-1}). Finally, the appropriate physico-chemical conditions must be present to produce a particular fabric. We identify the regions where olivine B-type fabric dominates based on the calculated results of temperature and stress distribution. For the typical magnitude of deviatoric stress in the models presented in this paper (0.1–10 MPa), the B–C transition temperature is around 700–800 °C (Fig. 2).

2. Viscous coupling between the slab and mantle wedge

When calculating temperature and stress profiles in the mantle wedge mantle of subduction zones, the kinematic boundary condition at slab–wedge interface plays an important role. We may have a fully coupled case where the velocity of material motion is continuous across this boundary. Alternatively, the slab and wedge may be only partially coupled with a large discontinuity in velocity across the slab–wedge interface. Partial coupling may be caused by localized viscous deformation of weak material such as sediments, serpentine, and talc or brittle sliding down dip from the seismogenic zone. The latter case is analogous to a situation with a brittle fault in a sheared viscous medium where deformation is accommodated by both short time scale brittle slip along the fault and long time scale viscous processes throughout the medium. If weak hydrated sediments give rise to partial coupling, the transition from partially coupling to full coupling could be controlled by a change in water content. We note that most of the sediments will be dehydrated at the depth of approximately 100 km. In the case of partial coupling associated with brittle slip, the brittle ductile transition (≈ 800 °C) controls the transition from partial to full viscous coupling.

Since we model only long time scale viscous processes we cannot account self-consistently for the non-seismic slip down-dip from the seismogenic zone. Furthermore, we use an olivine rheology that does not account for weaker material close to the slab–wedge interface. We make a simple approximation that non-viscous deformation and/or shear localization can be accounted for by reducing the magnitude of the velocity boundary condition along the slab–wedge interface in the forearc mantle (Fig. 3b).

We simulate three modes of slab–mantle coupling in the models presented in this paper: (1) full decoupling above 40 km with a velocity discontinuity between the slab and overriding plate, (2) a zone with reduced slab velocity between 40 and 70 km depth, and (3) full coupling between the slab and wedge below 70km. Note that the term 'decoupling' for the seismogenic zone is opposite to what is common in seismology, where the slab and overriding plate are considered coupled except during earthquake rupture.
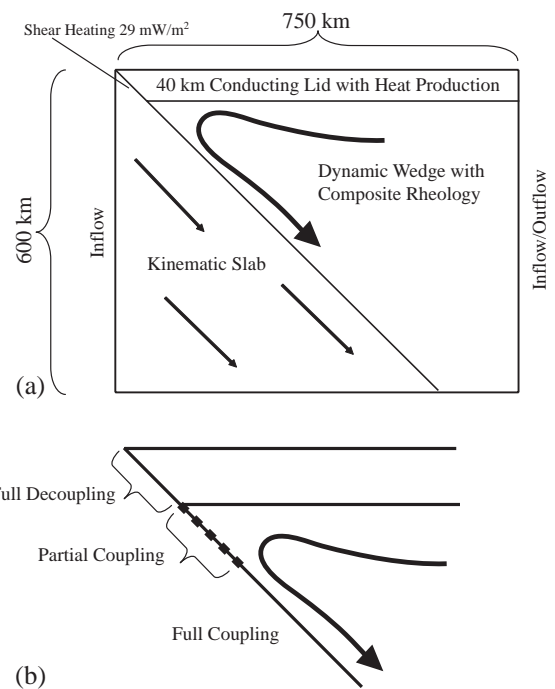

Fig. 3. Diagram showing the kinematic–dynamic setup and implemented features (a). Partial viscous coupling is simulated by modifying boundary conditions along the top of the slab (b).

3. Modeling approach

The models presented in this paper implement a kinematic–dynamic method where the slab and overriding lid are kinematically described and mantle wedge flow is dynamically modeled (Fig. 3a). Flow in the mantle wedge is driven by a kinematic boundary condition at the top of the slab. This is similar to the models described by [34–38]. We particularly follow the approach of [39]. We explore the rheological effects of water in steady-sate flow models by uniformly increasing water content in a region that radially extends 300 km from the corner point.

The finite element package SEPRAN is used for mesh generation and the numerical approximation of solutions for governing equations (http://ta.twi.tudelft.nl/sepran/sepran.html). The systems of equations generated by the finite element method are solved using a conjugate gradient iteration (Bi-CGSTAB) [40].

Flow in the mantle wedge is governed by the conservation of momentum for an incompressible infinite Prandtl number fluid without buoyancy forces:

$$-\nabla P + \nabla(\eta \cdot \dot{\boldsymbol{\epsilon}}) = 0 \qquad (1)$$

where $\dot{\boldsymbol{\epsilon}}$ is the strain rate tensor, η is effective viscosity, and P is dynamic pressure. The conservation of mass for an incompressible fluid is expressed as

$$\nabla \cdot u = 0 \qquad (2)$$

where u is velocity. Eqs. (1) and (2) are solved for pressure and velocity on a mesh composed of linear Taylor–Hood triangles [41].

A stress-free inflow/outflow boundary condition for Eq. (1) is present along the right hand boundary below 40 km. Velocity boundary conditions for Eq. (1) are prescribed along the top of the slab and at the base of the conducting lid. The velocity boundary condition is reduced along the top of the slab from
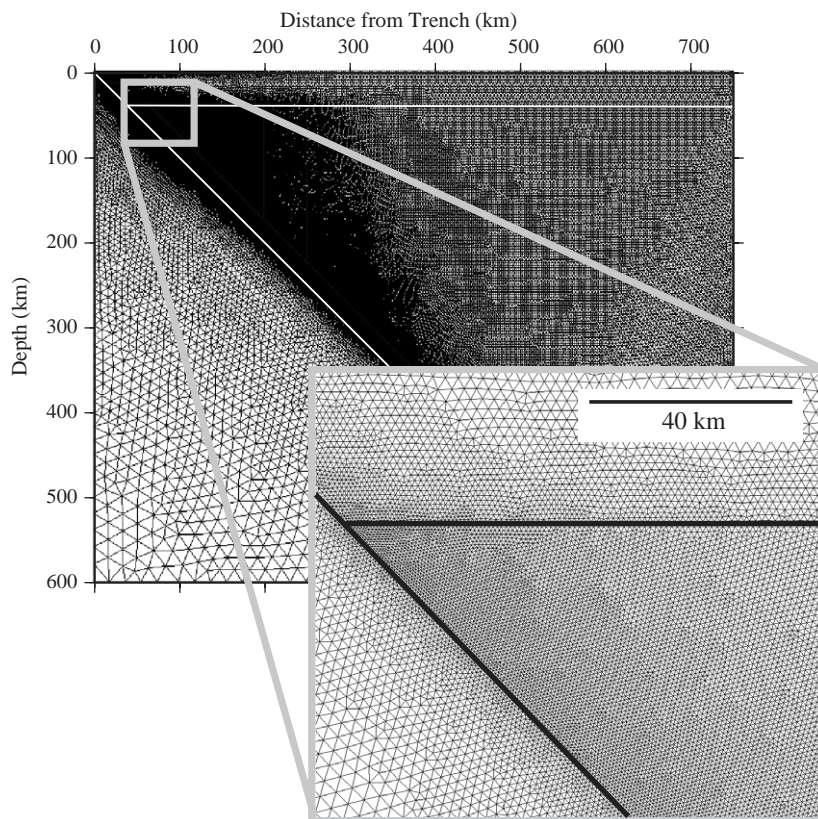

Fig. 4. Model domain and discretization.

the bottom of the conducting lid to around 70 km (Fig. 3b). The magnitude of the boundary condition is increased in a linear manner to slab velocity over 10 km along the slab surface. As discussed as above, this is a simple way to parameterize the effects of non-seismic slip and shear localization.

The conservation of energy for steady-state conditions takes the form of the convection–diffusion equation with heat production:

$$\rho c_{\mathrm{p}}(u \cdot \nabla)T = \nabla \cdot (k \nabla T) + Q + Q_{\mathrm{sh}} \quad (3)$$

where k is thermal conductivity, T is temperature, Q is radioactive heat production, Q_{sh} is shear heating, c_{p} is specific heat, and ρ is density. Specific heat is 1250 J/kg/K and density is 3300 kg/m^3. Shear heating is defined with a delta function:

$$Q_{\mathrm{sh}} = Q' \delta(x_{\mathrm{interface}}) \quad (4)$$

where Q' is the magnitude of shear heating, and $x_{\mathrm{interface}}$ is the position of the seismogenic zone. The seismogenic zone extends from the trench to the base of the conducting lid at 40 km and Q' is 29 mW/m^2. Heat production is 1.3 µW/m^3 from 0 to 15 km (upper crust) and 0.27 µW/m^3 from 15 to 30 km (lower crust). Streamline upwinding is used for the solution of Eq. (3) due to the strong advective term.

Fixed-temperature boundary conditions for the convection–diffusion equation are present along the top of the model ($T=0$), along the left inflow boundary (half-space cooling model), and along the right inflow boundary. The fixed temperature boundary condition along the upper 95 km of the right inflow boundary is described by a continental geotherm with crustal heat production as defined above and surface heat flow equal to 65 mW/m^2. A mantle potential temperature of 1450 °C is prescribed below 95 km to the depth of the outflow boundary condition.

Eqs. (1–3) are solved by the Picard iteration to relative accuracy of 10^{-6}. High resolution is necessary for accurate calculation of u and T because of large viscosity gradients in thermal boundary layers [39]. Resolution varies from 0.25 to 1 km in the forearc, back-arc mantle, and above the slab (Fig. 4). Viscosity varies within elements by less than a factor of 3. Slab dip is either 45° or defined by a polynomial fit to seismicity. Polynomial descriptions have smooth variation in curvature and produce more

accurate calculation of velocity for models with non-Newtonian rheology.

4. Rheology

A general steady-state rheological law for olivine at high temperatures can be expressed as

$$\dot{\epsilon}_{ij} = A\left(\frac{b}{d}\right)^m \exp\left[-\frac{(E+PV)}{RT}\right]\sigma^{n-1}\sigma_{ij} \quad (5)$$

where $\dot{\epsilon}_{ij}$ is the ij-th component of the strain rate tensor, σ_{ij} is the ij-th component of the deviatoric stress tensor, σ is the second invariant of the deviatoric stress tensor, b is the Burgers vector, d is grain size, E is activation energy, P is pressure, V is activation volume, R is the gas constant, T is temperature, n is the stress exponent, m is the grain size exponent, and A is a constant [42]. The strain rate tensor is defined as

$$\dot{\epsilon}_{ij} = \left(\frac{\partial u_i}{\partial x_j} + \frac{\partial u_j}{\partial x_i}\right). \quad (6)$$

Second invariants of the stress and strain rate tensors are defined as

$$\sigma = \sqrt{\frac{1}{2}\sum \sigma_{ij}\sigma_{ij}} \quad (7)$$

and

$$\dot{\epsilon} = \sqrt{\frac{1}{2}\sum \dot{\epsilon}_{ij}\dot{\epsilon}_{ij}} \quad (8)$$

respectively. Eqs. (7) and (8) are used to define an effective viscosity

$$\eta = \frac{\sigma}{\dot{\epsilon}} \quad (9)$$

For dislocation creep $m=0$ and $n>1$, which gives rise to a power-law rheology

$$\dot{\epsilon}_{ij} = A\exp\left[-\frac{(E+PV)}{RT}\right]\sigma^{n-1}\sigma_{ij}. \quad (10)$$

For computational purposes the effective viscosity for power-law rheology is defined in terms of $\dot{\epsilon}$ via the inversion of Eq. (10)

$$\eta_{\mathrm{disloc}} = A^{-\frac{1}{n}}\exp\left[\frac{(E+PV)}{RT}\right]\dot{\epsilon}^{\frac{1-n}{n}} \quad (11)$$

Table 1
Rheological parameters

$A_{\text{disloc, dry}}$	1.259×10^{-12} s^{-1} Pa^{-3}
$E_{\text{disloc, dry}}$	5.1×10^{5} J/mol
$V_{\text{disloc, dry}}$	14×10^{-6} m^3/mol
$A_{\text{disloc, wet}}$	3.631×10^{-18} s^{-1} Pa^{-3}
$E_{\text{disloc, wet}}$	4.1×10^{5} J/mol
$V_{\text{disloc, wet}}$	11×10^{-6} m^3/mol
$A_{\text{diff, dry}}$	1.088×10^{5} s^{-1} Pa^{-1}
$E_{\text{diff, dry}}$	3.0×10^{5} J / mol
$V_{\text{diff, dry}}$	6×10^{-6} m^3 / mol
$A_{\text{diff, sat}}$	6.625×10^{4} s^{-1} Pa^{-1}
$E_{\text{diff, sat}}$	2.4×10^{5} J / mol
$V_{\text{diff, sat}}$	5×10^{-6} m^3 / mol
n	3.0
r	1.2
q	1.2
b	0.5×10^{-9} m
d	1 mm
m	2.5
τ_y	100 MPa
$\dot{\epsilon}_y$	10^{-14} s^{-1}
n_y	5
$C_{\text{OH}}^{\max}$	5000 ppm H/Si

Newtonian diffusion creep has $n=1$ and $m>1$ which gives the following expression for effective viscosity

$$\eta_{\text{diff}} = A^{-1}\left(\frac{d}{b}\right)^m \exp\left[\frac{(E + PV)}{RT}\right]. \qquad (12)$$

Effective viscosity at low temperature is given by an approximated Peierls rheology

$$\eta_{\text{pei}} = \tau_y \dot{\epsilon}_y^{-\frac{1}{n_y}} \dot{\epsilon}^{\frac{1}{n_y}-1} \qquad (13)$$

where τ_y is a yield stress, $\dot{\epsilon}_y$ is a yield strain, and n_y is a constant [43] (Table 1). All three creep mechanisms occur in parallel which leads to the following effective composite viscosity

$$\eta = \left(\frac{1}{\eta_{\text{disloc}}} + \frac{1}{\eta_{\text{diff}}} + \frac{1}{\eta_{\text{pei}}}\right)^{-1}. \qquad (14)$$

The dislocation creep law is expressed in terms of parallel dry and wet mechanisms

$$\dot{\boldsymbol{\epsilon}} = \dot{\boldsymbol{\epsilon}}_{\text{disloc, dry}} + \dot{\boldsymbol{\epsilon}}_{\text{disloc, wet}} \qquad (15)$$

where

$$\dot{\boldsymbol{\epsilon}}_{\text{disloc, dry}} = A_{\text{disloc, dry}} \exp\left[-\frac{\left(E_{\text{disloc, dry}} + PV_{\text{disloc, dry}}\right)}{RT}\right]\sigma^n \qquad (16)$$

and

$$\dot{\boldsymbol{\epsilon}}_{\text{disloc, wet}} = A_{\text{disloc, wet}} C_{\text{OH}}^r \exp\left[-\frac{\left(E_{\text{disloc, wet}} + PV_{\text{disloc, wet}}\right)}{RT}\right]\sigma^n \qquad (17)$$

The concentration water in ppm H/Si is denoted by C_{OH}. Parameters for the dislocation creep law are for a closed system [44,45] (Table 1). The creep laws for dry and saturated diffusion creep [46,47] (Table 1) are combined into a law for conditions with variable water content [48]

$$\dot{\boldsymbol{\epsilon}} = \dot{\boldsymbol{\epsilon}}_{\text{diff, dry}} + \left(\dot{\boldsymbol{\epsilon}}_{\text{diff, sat}} - \dot{\boldsymbol{\epsilon}}_{\text{diff, dry}}\right)\left(\frac{C_{\text{OH}}}{C_{\text{OH}}^{\max}}\right)^q \qquad (18)$$

where

$$\dot{\boldsymbol{\epsilon}}_{\text{diff, dry}} = A_{\text{diff, dry}}\left(\frac{b}{d}\right)^m \exp\left[-\frac{\left(E_{\text{diff, dry}} + PV_{\text{diff, dry}}\right)}{RT}\right]\sigma \qquad (19)$$

and

$$\dot{\boldsymbol{\epsilon}}_{\text{diff, sat}} = A_{\text{diff, sat}}\left(\frac{b}{d}\right)^m \exp\left[-\frac{\left(E_{\text{diff, sat}} + PV_{\text{diff, sat}}\right)}{RT}\right]\sigma \qquad (20)$$

Dislocation creep dominates deformation for grain sizes around 1 mm and typical mantle wedge temperature and strain rate except in very cold low-strain–rate boundary layers. Grain sizes around 0.1 mm lead to fairly large regions dominated by diffusion creep where strain rate is moderate.

5. Results

We test several cases with a simple slab geometry: (1) dry composite rheology with full viscous coupling starting at a depth of 40 km, (2) wet composite rheology with 1000 ppm H/Si and full coupling at 40 km depth, and (3) wet composite rheology with 1000 ppm H/Si and partial coupling down to 70 km. Model parameters for each case can be found in Table 2.

Case 1 gives rise to very high temperatures in the forearc mantle wedge (Fig. 5). This is similar to the results of [39,49]. Temperature ranges from 1000 to

Table 2
Model parameters

Parameter	Case 1	Case 2	Case 3	Case 4	Case 5
Velocity (cm/yr)	8	8	8	9.1	9.1
Reduced velocity (cm/yr)	No reduction	No reduction	0.24	No reduction	0.27
Age of lithosphere (Ma)	50	50	50	130	130
Crustal conductivity (W/m/K)	3.1	3.1	3.1	2.5	2.5
Mantle conductivity (W/m/K)	3.1	3.1	3.1	3.1	3.1
Water content (ppm H/Si)	0	1000	1000	1000	1000
Slab geometry	45° dip	45° dip	45° dip	Polynomial	Polynomial

1250 °C which would facilitate melting in the mantle
50–60 km from the trench [37]. The combination of
high temperatures and non-Newtonian rheology pro-
duce a relatively low-stress environment (<3 MPa)
throughout the entire mantle wedge. Temperature
dependence of viscosity gives rise to the entrainment

of cold mantle-wedge material in the slab–wedge
interface and the focusing of cornerflow into the
corner point. Two low viscosity lobes develop in the
core of the wedge where strain rate is high.

A uniform water content of 1000 ppm H/Si [50] is
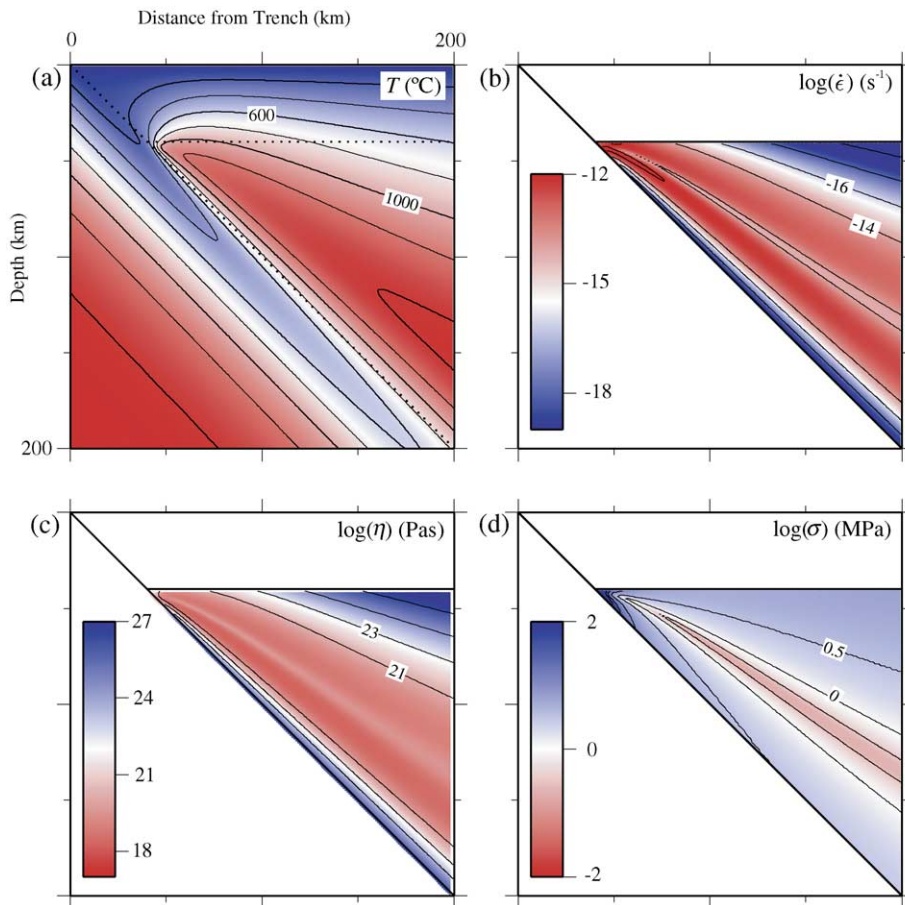added to the mantle wedge in Fig. 6. This uniform

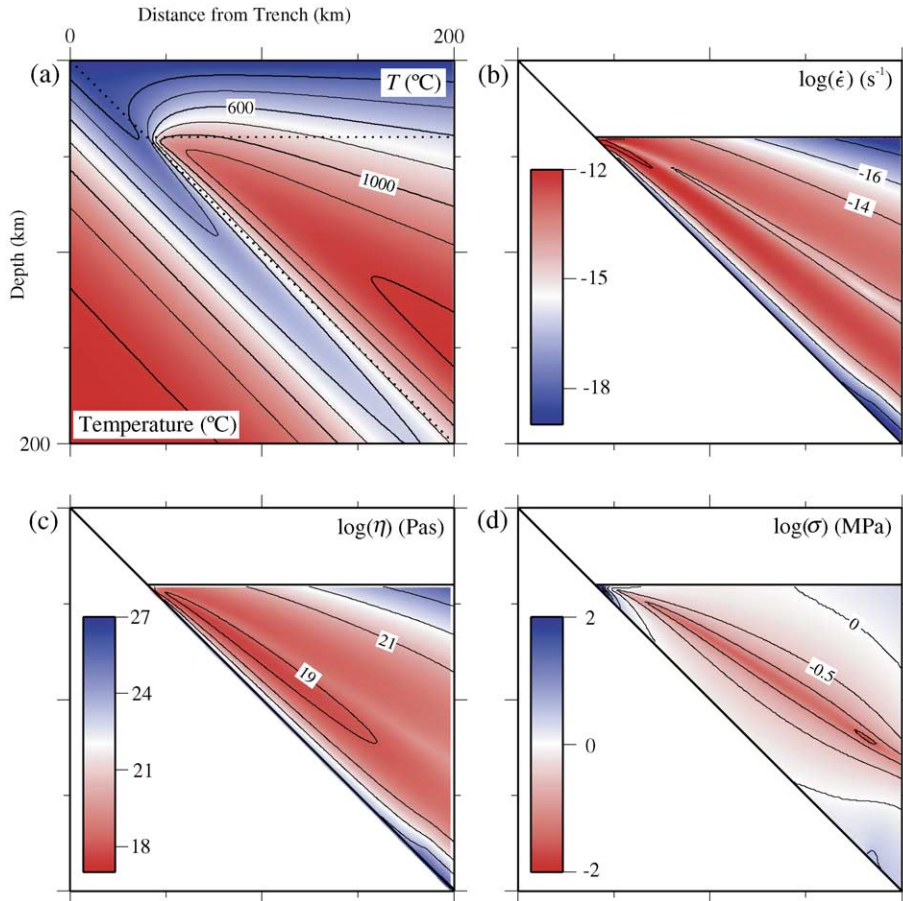Fig. 5. Steady-state calculations for temperature (a), strain rate (b), viscosity (c), and stress (d) for case 1.

Fig. 6. Steady-state calculations for temperature (a), strain rate (b), viscosity (c), and stress (d) for case 2.

concentration extends radially from the corner of the wedge to 300 km. This leads to a uniform viscosity reduction of around an order of magnitude, an increase in strain rate, and a stress reduction of around an order of magnitude. Stress is now less than 1 MPa for most of the mantle wedge. Increasing the water content to 3000 ppm and localizing the distribution of water to a 30 km layer above the slab does not modify the pattern of flow significantly. The low stress and high temperature observed for case 2 would hinder the development of B-type fabric.

The thermal structure of the forearc environment is modified considerably if the slab and forearc mantle are only partially coupled [51]. Partial viscous coupling limits the ability of the slab to entrain mantle in the slab–wedge interface thus decreasing the extent to which hot material can be focused into

the forearc mantle. Fig. 7 is an example of wet composite rheology with partial coupling between the slab and mantle down to 70 km. The depth at which the slab and mantle become fully coupled controls the height of penetration of the hot tongue of cornerflow, which is constrained to first order by the position of the volcanic front. A large temperature gradient from the wedge core to forearc mantle (30–40 °C/km) causes a rapid transition from conditions suitable for C-type fabric in the hot core of the mantle wedge to those more suitable for B-type in the forearc. This B–C transition occurs over 10–15 km. Lower temperatures in the forearc mantle wedge give rise to larger stress (50–70 MPa). However, more realistic low-temperature rheological models are necessary to model deviatoric stress accurately in the colder regions of the mantle wedge. If we
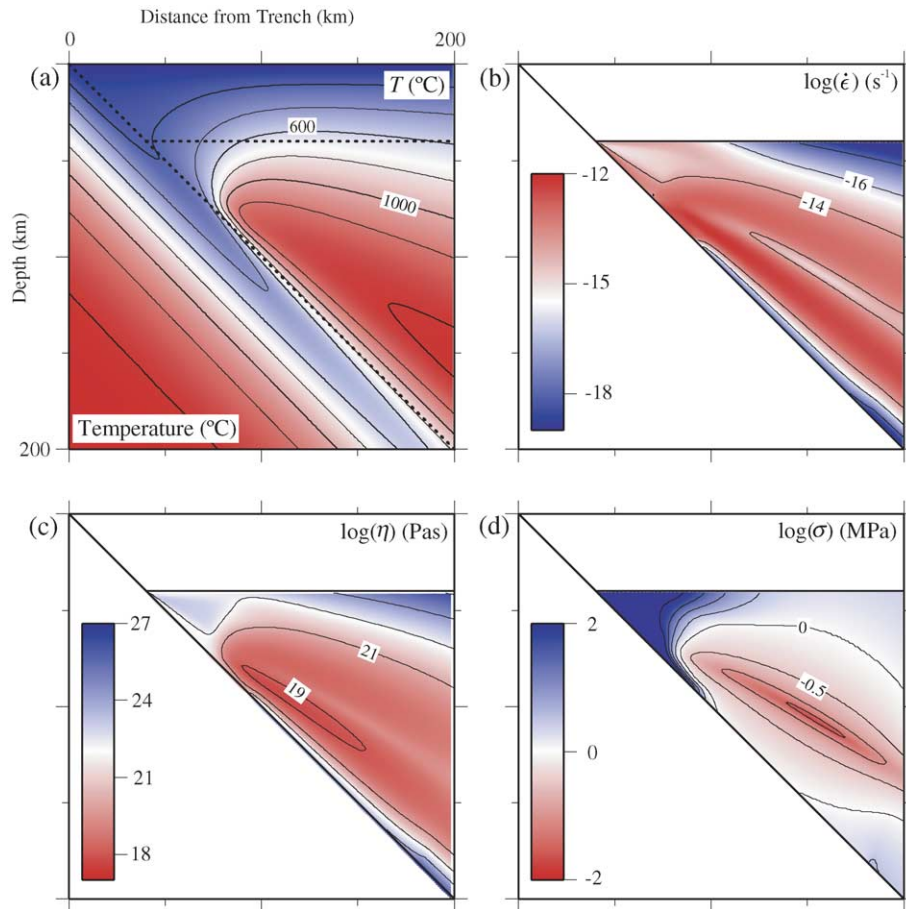
Fig. 7. Steady-state calculations for temperature (a), strain rate (b), viscosity (c), and stress (d) for case 3.

reduce the speed of subduction to around 3 cm/yr, the cold high-stress boundary layer thickens in the slab–wedge interface. Therefore conditions in this layer are also suitable for B-type fabric if subduction is moderately slow.

In cases 4 and 5 we use the geometry of the Honshu subduction system [39] (Fig. 8, Table 2). Case 4 with full coupling starting at the base of the 40 km conducting lid gives rise to a very shallow hot (1200 °C) tongue of mantle 80 km trenchward of the volcanic arc. Case 5 with partial viscous coupling between 40 and 70 km shows the low-temperature, high-stress nose similar to that observed in case 3. Case 5 also shows large temperature gradients (80 °C/ km) along the slab–wedge interface which corresponds to a maximum in intermediate depth seismic activity beneath Honshu [52].

6. Discussion

The thermal models presented in this work show that the thermal structure of the forearc mantle depends strongly on the depth of the transition from partial to full viscous coupling and the amount of partial coupling between the slab and forearc mantle. The up-slab position of the transition from the fully decoupled zone to possibly partially coupled zone with brittle and viscous deformation is marked by the maximum depth of large thrust earthquakes in the seismogenic zone. The down-slab position of the partial to full coupling transition cannot extend below the depth of the slab below the arc where significant viscous flow maintains high temperatures necessary for arc magmatism [35]. Models presented in this paper (Figs. 7 and 8) and previously published models
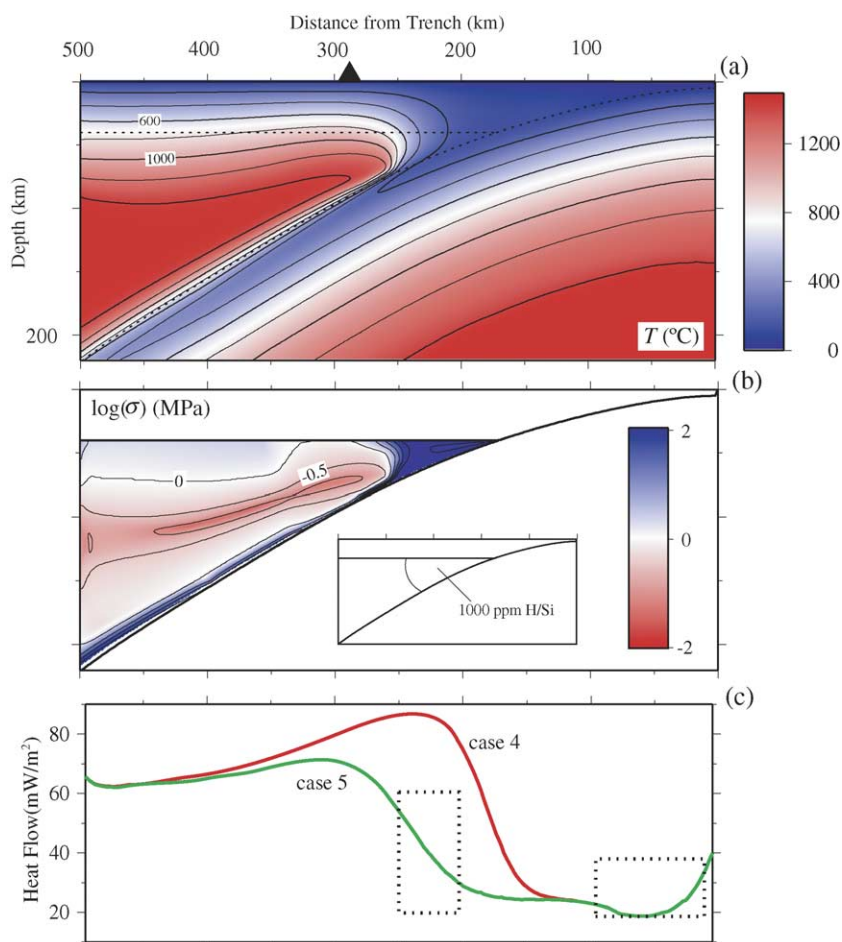
Fig. 8. Thermal and stress models of Honshu, Japan for 70 km partial viscous coupling (a and b). Dashed lines show the location of the top of the slab and base of the conducting lid. The volcanic front in denoted with a black triangle. Heat flow calculations are shown for cases 4 (red) and 5 (green) (c). Case 5 with partial viscous coupling down to 70 km produces a better match to observations, which are denoted with dashed boxes (data from [35]). Case 4 with full viscous coupling at the base of the 40 km conducting lid produces a poor match to forearc heat flow data.

[35,37,53] show that the full coupling point cannot be shallower than around 70 km to agree with heat flow [35], seismic attenuation, and velocity tomography [3,54–56].

Evidence for brittle deformation below the seismogenic zone comes from slow coseismic slip associated with large subduction zone earthquakes [57,58], periodic slow events [59], and persistent tremor [60]. Localizing such slow strain release was problematic before the advent of digital seismometry and modern geodesy surveys. Useful constraints may also come from the 26 December 2004 Sumatra–Andaman earth-

quake where a finite-rupture fault model can fit seismic waves at all frequencies but underpredicts geodetic displacements substantially [60–64].

Evidence for low-temperature conditions in the forearc mantle as shown by low heat flow, velocity and attenuation tomography, and the lack of forearc magmatism, suggests that convective flow in the forearc mantle is not too vigorous. Models presented in this paper show that calculated thermal structure is compatible with heat flow and seismic attenuation if the velocity boundary condition in the forearc mantle is less than 5% of slab velocity. For calculations with

greater coupling the forearc mantle becomes more open and convective heat transport produces high forearc heat flow and a poor match with seismic attenuation.

Partial viscous coupling in the slab–mantle interface may also be caused by the presence of low-temperature phyllosilicates such as talc and serpentine [65–68]. Both serpentine and talc are weak minerals and could cause shear localization in the slab–wedge interface. The abundance of low density serpentine may also facilitate viscous decoupling in the forearc. In this scenario a serpentinized forearc mantle is iso-

lated from large scale convective flow due to its positive buoyancy.

Models with deep partial coupling have suitable thermal and stress conditions for B-type fabric in the forearc mantle (Figs. 7, 8 and 9a). The core of the wedge is dominated by high-temperature, low-stress conditions that are more suitable for A-, C- or E-type fabric depending on water content. Increasing the depth of partial coupling from 70 to 100 km in the models shown in Figs. 7 and 8 produces a larger region with conditions suitable for B-type fabric
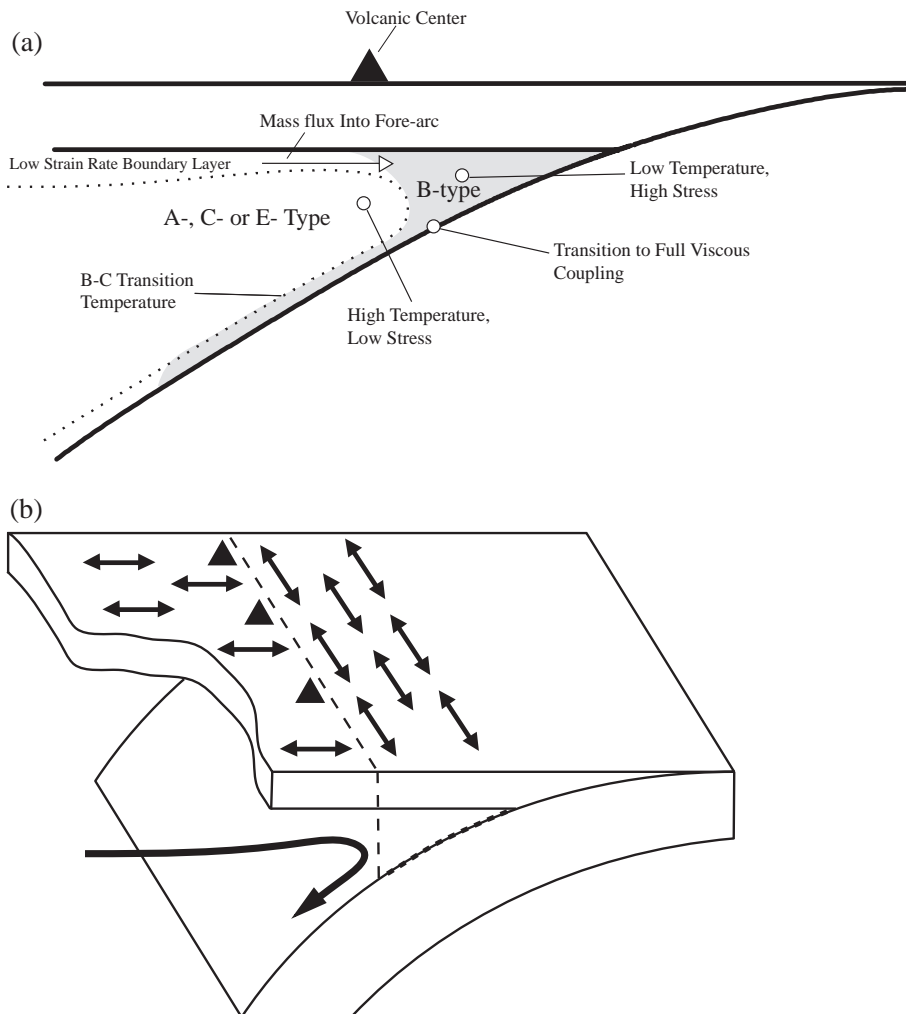

Fig. 9. Summary of model results showing candidate regions for B-type fabric (a). B-type fabric model for mantle wedge anisotropy (b). Predicted orientations of fast polarization is denoted with black double arrows (b). The transition from B-type conditions to conditions more suitable for C-type and other fabrics is denoted with a thin dashed line in (b). The thick dashed line along the surface of the slab shows the location of partial viscous coupling.

while satisfying heat flow and seismic attenuation and maintaining temperatures above the wet solidus in the mantle wedge below the arc.

When the rate of subduction is less than 3–4 cm/yr, the thickness of the thermal boundary layer above the slab increases to around 10–15 km. This layer is also a candidate for B-type fabric. Temperature in this boundary layer ranges from 700 to 1000 °C, which is close to the B–C transition temperature (800 °C) used to predict B-type fabric in this paper. However, the B–C transition occurs at higher temperature as stress increases (Fig. 2). Stress in the boundary layer above the slab could be higher than predicted by the models presented in this paper ($\approx$ 50 MPa). Stresses may be larger because we used a rather moderate yield stress for the low-temperature rheology. We note that this anisotropic interface is resolvable with Ps-scattering, where layer interfaces separated by 15-km can be resolved easily with 1-Hz waves [67].

The thin (10–15 km) possibly anisotropic layer above the slab will not produce large shear wave splitting (<0.1 s) (Fig. 9a). The forearc mantle, where we predict a larger region with B-type fabric, could yield a maximum splitting of 1 s. We expect that local shear waves will show smaller splitting toward the trench since the thickness of the forearc mantle decreases trenchward. The pattern of anisotropy associated with the predicted distribution of B-type fabric (Fig. 9a) is strongly dependent on the geometry of flow. Finite-strain calculations with simple 2D cornerflow geometry and isoviscous rheology [69] show large horizontal and vertical shear in the forearc mantle. Furthermore, our preliminary finite-strain calculations with composite rheology show stronger horizontal and vertical shear in the forearc mantle. This suggests that split shear waves from forearc regions will have trench-parallel fast polarization in simple subduction systems where flow geometry can be approximated by 2D cornerflow. For the simple 2D flow geometry, the position of the volcanic front is predicted to mark the transition from A-, C-, or E-type to B-type fabric and, consequently, from trench-perpendicular anisotropy in the back-arc and arc mantle to trench-parallel in the forearc mantle (Fig. 9a and 9b). This simple 2D model with olivine fabric transitions and horizontal and vertical shear has potential to explain trench-parallel shear wave splitting without including a complex flow geometry.

The sub-orthogonal convergence direction of the subducting Pacific plate and seismological observations from Northern Honshu [3,70] are consistent with the thermal and stress models and fabric distribution presented in this paper (Fig. 9a and b). Anisotropy in Northern Honshu shows an abrupt transition from trench-parallel fast directions in the forearc mantle to trench-perpendicular in the arc and back-arc [3]. A similar abrupt transition is observed in S-wave tomography where fast velocity in the forearc rapidly changes to slow velocity in the arc and back-arc mantle [3,52]. These rapid transitions in splitting direction and seismic velocity across the volcanic front are spatially similar to the rapid changes in temperature and stress that we predict with the models presented in this paper (Figs. 7 and 8). The general pattern of anisotropy shown in Fig. 9b is also observed in Central Andes [4,19], Hokkaido and along the transition from the Ryukyu arc to southern Kyushu [71]. Our models suggest that the regions with trench-parallel fast directions in these subduction systems are dominated by low temperatures, high stress, and B-type fabric.

Several subduction systems show trench-parallel shear wave splitting in the arc and back-arc mantle where we predict high-temperature and low-stress conditions that are not suitable for B-type fabric. These systems include Tonga [20], Eastern Aleutians [10], and Central Honshu [18]. Our models predict that a more probable cause for trench-parallel anisotropy in these subduction systems is trench-parallel flow with A-, C- or E-type fabric. Some subduction systems show fairly complex anisotropy. The pattern of shear wave splitting from sections of the Kamchatka [23] and Central Alaska subduction systems [72] is opposite to Fig. 9b (i.e. trench-perpendicular in the forearc and trench-parallel in the back-arc). If the component of trench-parallel shear is far greater than shear induced by the down going slab, B-type fabric may play an important role in these subduction zones by explaining the abrupt transition in fast polarization direction across the volcanic front. Trench-parallel shear in these subduction systems may be induced by flow around slab edges as proposed by [8,23]. Progress in three-dimensional modeling with temperature- and stress-dependent rheology is necessary to test the effects of more complex geometry and flow in the mantle wedge. We also note that the Cascadia subduc-

tion system shows trench-perpendicular fast directions in the forearc mantle [73] which suggests the presence of A-, E-, or C-type fabric. Thermal models of the Cascadia subduction system [38,39] suggest that temperature in the forearc mantle is appropriate for B-type fabric. This is in disagreement with the model presented in Fig. 9b. However, the trench-perpendicular forearc anisotropy observed by [73] may be caused by anisotropy within or beneath the slab since SKS phases were used in the study.

Further work in mineral physics and geodynamic modeling is needed to better understand the physical properties and behavior of materials in the cold forearc mantle. Future work will explore experimentally based low-temperature rheology and include viscous dissipation. These studies will help us better predict stress, temperature, deformation mechanisms, and strain in the mantle wedge and make more quantitative predictions. Preliminary models with viscous dissipation and more experimentally based low-temperature rheology give rise to similar results but with higher strain rate in the forearc mantle and temperature and stress in the B-type fabric stability field. If the forearc mantle is partially coupled, aseismic slip may occur at depth following large subduction thrust events. This motivates long-term geodetic monitoring of the region surrounding the $M > 9.0$ Sumatra–Andaman earthquake of 2004.

Questions also remain about whether or not enough strain can develop across the predicted B–C transition. Previous finite strain calculations for isoviscous rheology show greater than 600% strain accumulation for particles traveling through the forearc mantle [69]. The introduction of temperature- and stress-dependent viscosity increases strain accumulation by localizing deformation. Preliminary finite-strain calculations show greater than 200% strain accumulation across the predicted B–C transition for particles traveling into the forearc mantle from the low-strain–rate boundary layer below the overriding plate. This is a subject of future research.

7. Conclusions

We have developed steady-state subduction zone models with low-temperature forearc mantle deformation that are consistent with attenuation and velo-

city tomography and heat flow. Only minor viscous coupling between the slab and wedge in the forearc can exist in order to match observations. This sets an upper limit on the amount of deformation occurring in the forearc mantle. These models predict that temperature and stress in forearc mantle and slab–wedge interface are suitable for B-type fabric (Fig. 9a). This thin layer with B-type fabric above the slab will not produce significant shear wave splitting but may explain receiver function studies which show an anisotropic layer above the slab. The larger forearc mantle could produce splitting up to 1 s. This suggests that trench-parallel shear wave splitting in the forearc mantle of subduction zones can be explained by deformation associated with simple 2D corner-flow. This B-type fabric anisotropy hypothesis adequately predicts trench-parallel anisotropy without trench-parallel flow in the following subduction systems: Northern Honshu, Kyushu, Hokkaido, Ryukyu, and Central Andes. Our models also predict the rotation of fast direction from trench-parallel in the forearc to trench-perpendicular in the back-arc that is observed in these subduction systems. The core of the mantle wedge is characterized by high-temperature and low-stress conditions which are more suitable for A-, C-, or E-type fabrics depending on water content. Therefore we predict that trench-parallel shear wave splitting in the arc and back-arc mantle is more likely caused by A-, C-, or E-type fabrics with trench-parallel flow. If a significant component of trench-parallel shear is present in the arc and forearc mantle, than B-type fabric could also explain the pattern of anisotropy in parts of the Kamchatka and Alaska subduction systems.

References

[1] H. Jung, S. Karato, Water-induced fabric transition in olivine, Science 293 (2001) 1460–1463.

[2] I. Katayama, H. Jung, S. Karato, New type of olivine fabric from deformation experiments at modest water content and low stress, Geology 32 (2004) 1045–1048.

[3] J. Nakajima, A. Hasegawa, Shear-wave polarization aniso-tropy and subduction-induced flow in the mantle wedge of northeastern Japan, Earth Planet. Sci. Lett. 225 (2004) 365–377.

[4] M.L. Anderson, G. Zandt, E. Triep, M. Fouch, S. Beck, Anisotropy and mantle flow in the Chile–Argentina subduc-tion zone from shear wave splitting analysis, Geophys. Res. Lett. 31 (2004), doi:10.1029/2004GL020906.

[5] D.A. Wiens, G.P. Smith, Seismological constraints on the structure and flow patterns within the mantle wedge, in: J. Eiler (Ed.), Inside the subduction factory, Geophysical Mono-graph, vol. 138, AGU, Washington, D.C, 2003, pp. 83–105.

[6] P.E. van Keken, The structure and dynamics of the mantle wedge, Earth Planet. Sci. Lett. 215 (2003) 323–338.

[7] M.K. Savage, Seismic anisotropy and mantle deformation: what have we learned from shear wave splitting? Rev. Geo-phys. 37 (1999) 65–106.

[8] J. Park, V. Levin, Seismic anisotropy: tracing plate dynamics in the mantle, Science 296 (2002) 485–489.

[9] M.J. Fouch, K.M. Fischer, Shear wave anisotropy in the Mariana subduction zone, Geophys. Res. Lett. 25 (1998) 1221–1224.

[10] X. Yang, K.M. Fischer, G. Abers, Seismic anisotropy beneath the Shumagin Islands segment of the Aleutian–Alaska sub-duction zone, J. Geophys. Res. 100 (1995) 18165–18177.

[11] A.L. Littlejohn, H.J. Greenwood, Lherzolite nodules in basalts from British Columbia, Canada, Can. J. Earth Sci. 11 (1996) 1288–1308.

[12] B.W. Ismaïl, D. Mainprice, An olivine fabric database: an overview of upper mantle fabrics and seismic anisotropy, Tectonophysics 196 (1998) 145–157.

[13] K. Frese, V. Trommsdorff, K. Kunze, Olivine [100] normal to foliation: lattice preferred orientation in prograde garnet peri-dotite formed at high H_2O activity, Cima di Gagnone (Central Alps), Contrib. Mineral. Petrol. 145 (2003) 75–86.

[14] L. Mehl, B.R. Hacker, G. Hirth, P.B. Kelemen, Arc-parallel flow within the mantle wedge evidence from the accreted Talkeetna arc, south central Alaska, J. Geophys. Res. 108 (2003), doi:10.1029/2002JB002233.

[15] T. Sawaguchi, Deformation history and exhumation process of the Horoman Peridotite Complex, Hokkaido, Japan, Tectono-physics 379 (2004) 109–126.

[16] T. Mizukami, S.R. Wallis, J. Yamamoto, Natural examples of olivine lattice preferred orientation patterns with a flow–nor-mal *a*-axis maximum, Nature 427 (2004) 432–436.

[17] T. Tamimoto, D. Anderson, Mapping convection in the mantle, Geophys. Res. Lett. 11 (1984) 287–290.

[18] Y. Hiramatsu, M. Ando, T. Tsukuda, T. Ooida, Three-dimen-sional image of the anisotropic bodies beneath central Honshu, Japan, Geophys. J. Int. 135 (1998) 801–816.

[19] J. Polet, P.G. Silver, S. Beck, T. Wallace, G. Zandt, S. Ruppert, R. Kind, A. Rudloff, Shear wave anisotropy beneath the Andes from the BANJO, SEDA, and PISCO experiments, J. Geo-phys. Res. 105 (2000) 6287–6304.

[20] G.P. Smith, D.A. Wiens, K.M. Fischer, L.M. Dorman, S.C. Webb, J.A. Hildebrand, A complex pattern of mantle flow in the Lau Back arc, Science 292 (2001) 713–716.

[21] V. Peyton, V. Levin, J. Park, M. Brandon, M. Lees, E. Gordeev, A. Ozerov, Mantle flow at slab edge: seismic aniso-tropy in the Kamchatka region, Geophys. Res. Lett. 28 (2001) 379–382.

[22] V. Levin, J. Park, J. Lees, M.T. Brandon, V. Peyton, E. Gordeev, A. Ozerov, Crust and upper mantle of Kamchatka from teleseismic receiver functions, Tectonophysics 358 (2002) 233–265.

[23] V. Levin, D. Drozin, E. Gordeev, Detailed mapping of seismic anisotropy with local shear waves in southeastern Kamchatka, Geophys. J. Int. 158 (2004) 1009–1023.

[24] C.E. Hall, K.M. Fischer, E.M. Parmentier, D.K. Blackman, The influence of plate motions on three-dimensional back arc mantle flow and shear wave splitting, J. Geophys. Res. 105 (2000) 28009–28033.

[25] S. Karato, Mapping water content in the upper mantle, in: J. Eiler (Ed.), Inside the subduction factory, Geophysical Mono-graph, vol. 138, AGU, Washington, D.C, 2003, pp. 135–149.

[26] B.K. Holtzman, D.L. Kohlstedt, M.E. Zimmerman, F. Heidel-back, T. Hiraga, J. Hustoft, Melt seg-regation and strain parti-tioning: implications for seismic anisotropy and mantle flow, Science 301 (2003) 1227–1230.

[27] S. Zhang, S. Karato, J.F. Gerald, U.H. Faul, Y. Zhou, Simple shear deformation of olivine aggregates, Tectonophysics 316 (2000) 133–152.

[28] M. Bystricky, K. Kunze, L. Burlini, J.P. Burg, High shear strain of olivine aggregates: Rheological and seismic conse-quences, Science 290 (2000) 1564–1567.

[29] S. Karato, Microscopic models for the influence of hydrogen on physical and chemical properties of minerals, in: D.A. Yuen, S. Maruyama, S. Karato, B.F. Windley (Eds.), Super-plume: Beyond Plate Tectonics, Springer, In press.

[30] J.R. Möckel, Structural petrology of the garnet-peridotite of Alpe Arami (Ticino, Switzerland), Leidse Geologische 42 (1969) 61–130.

[31] F. Cordellier, F. Boudier, A.M. Boullier, Structural study of the Almklovdalen peridotite massif (Southern Norway), Tectono-physics 77 (1981) 257–281.

[32] P. Skemer, I. Katayama, S. Karato. B-type olivine fabric from the Cima di Gagnone, central Alps, Geology, (submitted for publication).

[33] I. Katayama, S. Karato. Effects of temperature and stress on the deformation fabrics of olivine under hydrous conditions: An experimental study, Earth Planet. Sci. Lett., (submitted for publication).

[34] J.H. Davies, D.J. Stevenson, Physical model of source region of subduction zone volcanics, J. Geophys. Res. 97 (1992) 2037–2070.

[35] Y. Furukawa, S. Uyeda, Thermal structure under the Tohoko arc with consideration of crustal heat generation, Tectonophy-sics 164 (1989) 175–187.

[36] S.M. Peacock, K. Wang, Seismic consequences of warm ver-sus cool subduction metamorphism: examples from southwest and northeast Japan, Science 286 (1999) 937–939.

[37] J.A. Conder, D. Wiens, J. Morris, On the decompression melt-ing structure at volcanic arcs and back-arc spreading centers, Geophys. Res. Lett. 29 (2002), doi:10.1029/2002GL015390.

[38] C.A. Currie, K. Wang, R.D. Hyndman, J. He, The thermal effects of steady-state mantle flow above a subducting plate: the Cascadia subduction zone and back arc, Earth Planet. Sci. Lett. 223 (2000) 35–48.

[39] P.E. van Keken, B. Kiefer, S.M. Peacock, High-resolution models of subduction zones: implications for mineral dehydration reactions and the transport of water into the deep mantle, Geochem. Geophys. Geosyst. 3 (2002), doi:10.1029/2001DC000256.

[40] H.A. van der Vorst, Bi-CGSTAB: a fast and smoothly converging variant of Bi-CG for the solution of nonsymmetric linear systems, SIAM J. Sci. Comput. 12 (1992) 631–644.

[41] C. Cuvelier, A. Segal, A.A. van Steenhoven, Finite Element Methods and Navier–Stokes Equations, Reidel Publishing, Dordrecht, Holland, 1986, p. 483.

[42] G. Ranalli, Rheology of the Earth: Deformation and Flow Processes in Geophysics and Geodynamics, Allen and Unwin, Boston, 1987, p. 366.

[43] H. Čížková, J. van Hunen, A.P. van den Berg, N.J. Vlaar, The influence of rheological weakening and yield stress on the interaction of slabs with the 670 km discontinuity, Earth Planet. Sci. Lett. 199 (2002) 447–457.

[44] S. Karato, H. Jung, Effects of pressure on high-temperature dislocation creep in olivine, Philos. Mag. 83 (2003) 401–414.

[45] S. Mei, D.L. Kohlstedt, Influence of water on plastic deformation of olivine aggregates: 2. Dislocation creep regime, J. Geophys. Res. 105 (2000) 21471–21481.

[46] S. Karato, P. Wu, Rheology of the upper mantle: a synthesis, Science 260 (1993) 771–778.

[47] S. Mei, D.L. Kohlstedt, Influence of water on plastic deformation of olivine aggregates: 1. Diffusion creep regime, J. Geophys. Res. 105 (2000) 21457–21469.

[48] S. Franck, C. Bounama, Effects of water dependent creep rate on volatile exchange between mantle and surface reservoirs, Phys. Earth Planet. Inter. 92 (2000) 57–65.

[49] P.B. Kelemen, J.L. Rilling, E.M. Parmentier, L. Mehl, B.R. Hacker, Thermal structure due to solid-state flow in the mantle wedge beneath arcs, in: J. Eiler (Ed.), Inside the subduction factory, Geophysical Monograph, vol. 138, AGU, Washington, D.C, 2003, pp. 293–311.

[50] G. Hirth, D. Kohlstedt, Rheology of the upper mantle and the mantle wedge: a view from the experimentalists, in: J. Eiler (Ed.), Inside the subduction factory, Geophysical Monograph, vol. 103, AGU, Washington, D.C, 2003, pp. 83–105.

[51] Y. Furukawa, Depth of the decoupling plate interface and thermal structure under arcs, J. Geophys. Res. 98 (1993) 20005–20013.

[52] H. Zhang, C.H. Thurber, D. Shelly, I. Satoshi, G.C. Beroza, A. Hasegawa, High-resolution subducting-slab structure beneath northern Honshu, Japan revealed by double-difference tomography, Geology 32 (2004) 361–364.

[53] J.A. Conder, A case for hot slab surface temperatures in numerical viscous flow models of subduction zones with improved fault zone parameterization, Phys. Earth Planet. Inter. 149 (2005) 155–164.

[54] N. Tsumura, S. Matsumoto, S. Horiuchi, A. Hasegawa, Three-dimensional attenuation structure beneath the northeastern Japan arc estimated from spectra of small earthquakes, Tecontophysics 319 (2000) 241–260.

[55] T. Takanami, I.S. Sacks, A. Hasegawa, Attenuation structure beneath the volcanic front in northeastern Japan from broad-band seismograms, Phys. Earth Planet. Inter. 121 (2000) 339–357.

[56] J.C. Stachnik, G.A. Abers, D. Christensen, Seismic attenuation and mantle wedge temperatures in the Alaska subduction zone, J. Geophys. Res. 109 (2004), doi:10.1029/2004JB003018.

[57] H. Kanamori, C.J.J., Focal process of the great Chilean earthquake May 22, 1960, Phys. Earth Planet. Int. 9 (1974) 128–136.

[58] E. Bonafede, M. Boschi, M. Dragoni, Mechanical models of slow source processes, in: H. Kanamori, E. Boschi (Eds.), Earthquakes; Observation, Theory and Interpretation, Scuola Inter-nazionale di Fisica Enrico Fermi, North Holland, Amsterdam, 1983, pp. 330–344.

[59] G. Rogers, H. Dragert, Episodic tremor and slip on the Cascadia subduction zone: the chatter of silent slip, Science 300 (2003) 1942–1943.

[60] K. Obara, Nonvolcanic deep tremor associated with subduction in southwest Japan, Science 296 (2002) 1679–1681.

[61] C.J. Ammon, C. Ji, H.K. Thio, D. Robinson, S. Ni, V. Hjorleifsdottir, H. Kanamori, T. Lay, S. Das, G. Helmberger, G. Ichinose, J. Polet, D. Wald, Rupture process of the 2004 Sumatra–Andaman earthquake, Science 308 (2005) 1133–1139.

[62] J. Park, T.R. Song, J. Tromp, E. Okal, S. Stein, G. Roult, E. Clevede, G. Laske, H. Kanamori, P. Davis, J. Berger, C. Braitenberg, M. Van Camp, X. Lei, H. Sun, R.S. Xu, H., Earth's free oscillations excited by the 26 December 2004 Sumatra–Andaman earthquake, Science 308 (2005) 1139–1144.

[63] T. Lay, H. Kanamori, C.J. Ammon, M.M. Nettles, S.N. Ward, R.C. Aster, S.L. Beck, S.L. Bilek, M.R. Brudzinski, R. Butler, H.R. DeShon, G. Ekstrom, K. Satake, S. Sipkin, The great Sumatra–Andaman earthquake of 26 December 2004, Science 302 (2005) 1127–1133.

[64] R. Bilham, A flying start, then a slow slip, Science 308 (2005) 1126–1127.

[65] S.M. Peacock, R.D Hyndman, Hydrous minerals in the mantle wedge and the maximum depth of subduction thrust earthquakes, Geophys. Res. Lett. 26 (1999) 2517–2520.

[66] A.G. Bostock, R.D. Hyndman, S. Rondenay, S.M. Peacock, An inverted continental Moho and serpentinization of the fore arc mantle, Nature 417 (2002) 536–538.

[67] J. Park, H. Yuan, V. Levin, A serpentinite skidmark of trench-parallel terrane migration? J. Geophys. Res. 109 (2004), doi:10.1029/2003JB002718.

[68] R. Blakely, T. Brocher, R. Wells, Subduction-zone magnetic anomalies and implications for hydrated forearc mantle, Geology 33 (2005) 445–448.

[69] D. McKenzie, Finite deformation during fluid flow, Geophys. J. R. Astron. Soc. 58 (1979) 689–715.

[70] T. Okada, T. Matsuzawa, A. Hasegawa, Shear-wave polarization anisotropy beneath the north-eastern part of Honshu, Japan, Geophys. J. Int. 123 (1995) 781–797.

[71] M.D. Long, R.D. van der Hilst, Upper mantle anisotropy beneath Japan from shear wave splitting, Phys. Earth Planet. Inter. 151 (2005) 206–222.

[72] D.H. Christensen, G.A. Abers, T. McNight, Mantle anisotropy beneath the Alaska range inferred from S-wave splitting observations: results from BEAAR, EOS Trans. AGU 84 (2003) (Fall Meet. Suppl., Abstract S31C–0782).

[73] C.A. Currie, J.F. Cassidy, R.D. Hyndman, M.G. Bostock, Shear wave anisotropy beneath the Cascadia subduction zone and western North American craton, Geophys. J. Int. 157 (2004) 341–353.